11th World Congress on Computational Mechanics (WCCM XI)
5th European Conference on Computational Mechanics (ECCM V)
6th European Conference on Computational Fluid Dynamics (ECFD VI)
E. Oñate, J. Oliver and A. Huerta (Eds)

AN OPTIMIZATION OF TURBULENT FLOWS BY USING DATA ASSIMILATION

HIROSHI KATO*

* Institute of Aeronautical Technology
Japan Aerospace Exploration Agency
7-44-1, Jindaiji Higashi-machi, Chofu-shi, Tokyo 182-8522, Japan
e-mail: kato.hiroshi@jaxa.jp

Key Words: *Turbulent flows, Uncertainty, Data Assimilation, Optimization.*

Abstract. In this study, the ensemble transform Kalman filter, a sequential advanced data assimilation method, is employed to estimate the angle of attack, the Mach number, and the turbulent viscosity corresponding with the experimental pressure coefficients of the transonic flow around the ONERA M6 wing. As the result, the computation with the angle of attack, the Mach number, and the turbulent viscosity estimated by the ETKF improves discrepancies between original computations and the experiment. This result suggests that data assimilation is effective to estimate proper turbulent flow conditions by combining computational data and experimental data with data assimilation.

1 INTRODUCTION

Experimental fluid dynamics (EFD) and computational fluid dynamics (CFD) are major tools for aerodynamic designs in the field of aeronautical engineering. In the aeronautical engineering, EFD employs a wind tunnel facility and CFD employs a high-speed computer such as a supercomputer. However, as wind tunnel experiments and computers are just facilities on the ground, EFD and CFD have many uncertainty factors to represent flows around flying aircrafts or space crafts. Figure 1 shows uncertainty factors of EFD and CFD. These uncertainty factors become obstacles to estimate accurate aerodynamic characteristics when flow fields are complicated.

An example of the uncertainty factors is an angle of attack. The angle of attack is one of boundary conditions. In most cases, angle of attacks of experiments are corrected to eliminate wind tunnel wall interference, and corrections are conducted with empirical formulae. However, different empirical formulas are employed for each wind tunnel test case, therefore, there is a possibility that sufficient corrections are not employed to obtain proper angle of attacks. Moreover, angle of attacks of computations are not necessarily correspond to corrected angle of attacks of experiments. Another example of the uncertainty factors is a turbulence model. The turbulence model is a computational method to represent turbulent flows efficiently. To date, several turbulence models have been proposed, and the effectiveness have been shown. However, turbulence models predict different turbulent flows for complex turbulent flows, and then the choice of the turbulence model has significant

effects on computational results.

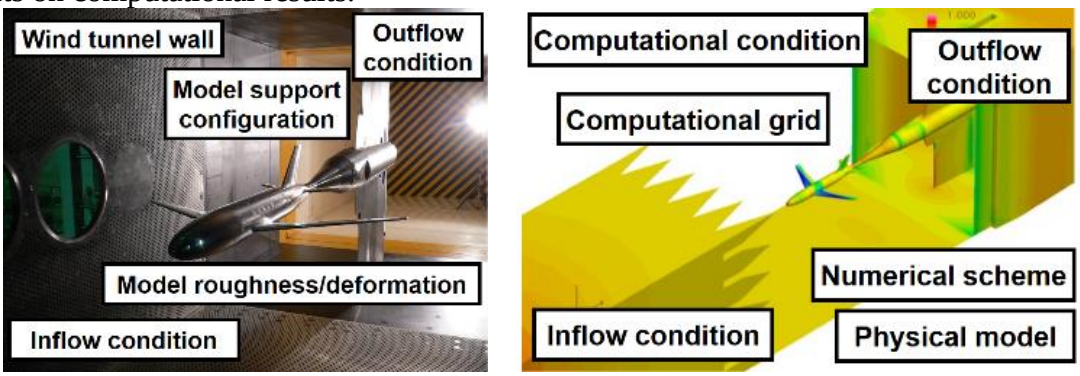

(a) EFD (b) CFD

Figure 1: Example of uncertainty factors of EFD and CFD

Recently, understanding of complex turbulent flows becomes increasingly important as a means of designing of high-efficiency aircrafts and space crafts. However, current experimental and computational approaches have difficulties in representing complex turbulent flows. The one of reasons arises from uncertainty factors of EFD and CFD. However, uncertainty quantifications for flow analysis have not been conducted sufficiently, because flow analysis is a kind of extreme large scale and non-linearly problems. Therefore, an approach with considering the uncertainty factors will be an important tool to represent complex turbulent flows.

The Kalman filter [1] is well known as one of approaches with considering uncertainties of measured data and computational data. The Kalman filter is based on the Bayesian estimation, uncertainties of measured data and computational data are employed to obtain realistic data. However, the Kalman filter is not applied to analysis of fluid. The major problem is that CFD employs a strong nonlinear system model, the Navier–Stokes equations, to analyze fluid problems.

Here, there is the data assimilation methodology [2,3] in the field of earth science. Data assimilation has been widely used to estimate initial and boundary conditions for numerical weather predictions. In the numerical weather predictions, the Navier–Stokes equations is employed as the system model, as well as in the field of aeronautical designs. Hence, data assimilation methodology can be applied to analyze fluid problems in the field of aeronautical engineering. In addition, data assimilation can represent realistic data combining measured data and computational data. As current experimental and computational approaches cannot represent complex turbulent flows sufficiently, realistic complex turbulent flows represented by data assimilation can contribute for aerodynamic designs as a new information.

In this study, an advanced sequential data assimilation technique, the ensemble transform Kalman filter (ETKF) [4], is applied to obtain realistic flow field combining measured data and computational data, and the effectiveness is investigated. To show the effectiveness suggests that data assimilation becomes an important tool in the field of engineering.

The rest of the paper is organized as follows. Section II describes the problem setting. Section III describes the method. Then, the data assimilation procedure is shown in Section IV. Section V presents the results. Finally, the conclusions are given in Section VI.

2 PROBLUEM SETTING

2.1 Flow conditions

In this study, a transonic flow around the ONERA M6 wing was employed for data assimilation. The flow conditions are the Reynolds number of 11.7 million, the Mach number of 0.8395, and an angle of attack of 6.06 degree. In the flow condition, there is a discrepancy between measured data and computational data as shown in Fig. 2. Figure 2 shows a comparison of pressure coefficients around on the wing tip between the experimental data and computed results. In the computations, the Spalart–Allmaras turbulence model (SA) [5] and the Menter SST turbulence model (SST) [6] were employed with the CFL number of 50. The comparisons were conducted at the spanwise distances of z/b = 0.95 and 0.99 (b: wing span length).

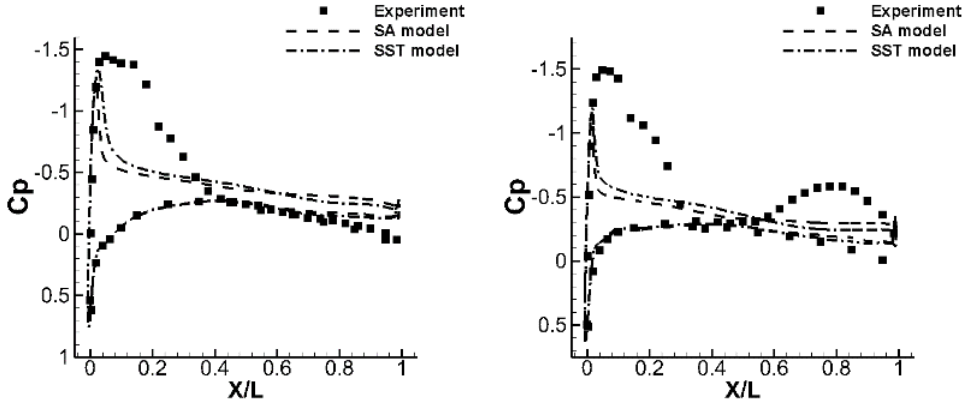

(a) z/b = 0.95 (b) z/b = 0.99

Figure 2: Comparison of pressure coefficients on the wing surface

2.2 Role of data assimilation

This study focuses on an angle of attack, the Mach number, and a turbulence model as uncertainty factors of CFD. In addition, uncertainties of measurement data are not considered. Thus, data assimilation aims to correct original computational data to fit better with the flow corresponding with the measurement data. This enables to avoid discussions about whether reconstructed data by data assimilation under both uncertainty of measurement data and computational data is proper or not. In addition, the reconstructed data corresponding with the measurement data becomes an important indicator to show an effectiveness of data assimilation. This can be effective to show easily the effectiveness of data assimilation.

Furthermore, this study does not investigate which turbulence model is best. This study investigates the best turbulent viscosity, which is determined by eddy viscosity type turbulence models. The best turbulent viscosity estimated by data assimilation will be helpful to design the next best eddy viscosity type turbulence model.

3 METHOD

3.1 System model

In this study, a CFD code called the fast aerodynamic routine (FaSTAR) [7] developed in Japan Aerospace Exploration Agency (JAXA) was employed to obtain computational data. The computation was performed with the CFL number of 50, and Table 1 shows the representative computational schemes employed in this study.

Table 1: Computational methods employed in this study

Invisid flux	HLLEW [8]
Gradient	GLSQ [9]
Limiter	Hishida's limiter
Viscous flux	Cell gradient
Time integration	GMRES

Figure 3 shows the computational grid employed in this study. The number of nodes of the computational grid was 678053, and the minimum grid spacing was 1.d-5 (the representative length of the computational grid was set to be 1 at the mean line of the wing). The effect of minimum grid spacing on the computational result was investigated before starting this study.

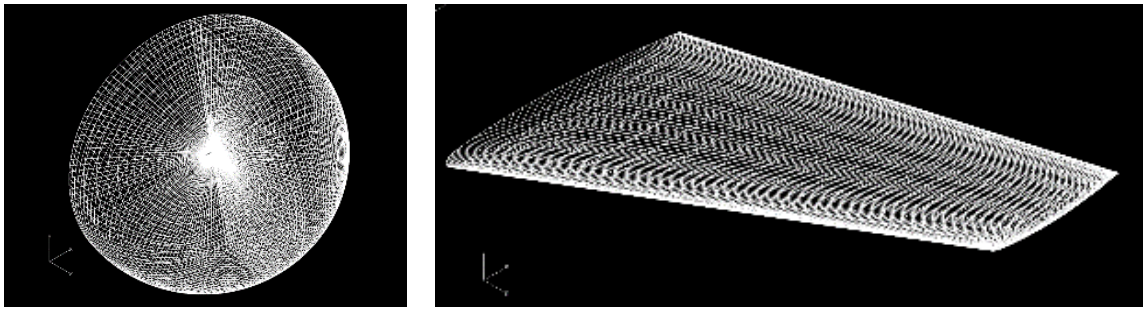

(a) Whole domain (b) Wing surface

Figure 3: Computational grid employed in this study

Next, state variables in the system model were modified to estimate an angle of attack, the Mach number, and turbulent viscosity. In a computation with an eddy viscosity turbulence model, original state variables consist of density ρ, velocity components u, v, w, pressure p, and state variables, which are required in an eddy viscosity turbulence model. When the Spalart–Allmaras turbulence model that uses $\tilde{\nu}$ as variables is employed as a turbulence model, the state variables are expressed in Eq. (1). Turbulent viscosity is calculated secondarily from the state variables.

$$\boldsymbol{x}_t = (\rho \quad u \quad v \quad w \quad p \quad \tilde{\nu})^T, \tag{1}$$

where $\boldsymbol{x}$ shows the state vector in the system model, subscript t represents the index of time steps, and superscript T represents the transposed matrix.

Here, in this study, turbulent viscosity is directly estimated by the ETKF. Therefore,

variables of a turbulence model are not required for the state variables, and the variables of the turbulence model are replaced by turbulent viscosity as in Eq. (2).

$$\boldsymbol{x}_t = (\rho \quad u \quad v \quad w \quad p \quad \mu_t)^T, \tag{2}$$

In addition, an angle of attack α and the Mach number M are estimated by data assimilation along with turbulent viscosity. Therefore, an angle of attack and the Mach number are added to the state variables as in Eq. (3).

$$\boldsymbol{x}_t = (\rho \quad u \quad v \quad w \quad p \quad \mu_t \quad \alpha \quad M)^T, \tag{3}$$

3.2 Experimental data

In this study, surface pressures on the wing were employed as experimental data. The experimental pressure coefficients on the wing surface from the wind tunnel experiment have been released on the research paper [10]. The number of experimental data available in [10] was 281.

In this study, since the pressure was utilized as experimental data, the pressure coefficients were converted to the non-dimensional pressure using Eq. (4).

$$C_p = \frac{\left(p - \frac{1}{\gamma}\right)}{\frac{1}{2}M^2}, \tag{4}$$

where p is the non-dimensional pressure, C_p is the pressure coefficient, γ is the specific heat ratio of 1.4, and M is the Mach number of 0.8395.

In addition, the experimental data far from the computational grid points were not employed for data assimilation. The experimental data not employed for data assimilation were employed to investigate the data assimilation result. Finally, the number of experimental data employed for data assimilation was 159. The measurement was conducted at seven wing sections in Table 2. Figure 4 shows positions to measure pressure coefficients on the wing surface.

Table 2: Spanwise locations for measurement

Section	z/b (b: wing span length)
1	0.2
2	0.44
3	0.65
4	0.8
5	0.9
6	0.95
7	0.99

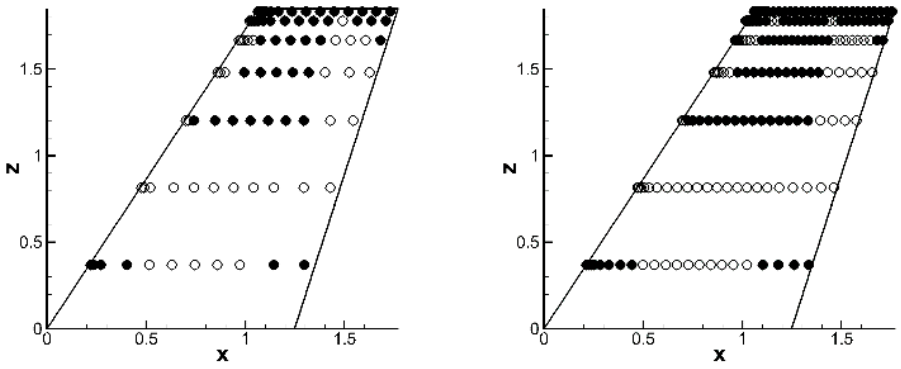

(a) Lower wing surface (b) Upper wing surface

Figure 4: Positions to measure pressure coefficients on the wing surface (●: positions employed for data assimilation)

3.3 ETKF

The ETKF is a sequential data assimilation method. The mathematical backgrounds of these methods are based on the minimum error variance assumption as the Kalman filter. In the ETKF, the filtered mean and variance that appear in the Kalman filter are replaced by obtaining a set of ensemble members. The mean matrix of ensemble members $\widehat{\boldsymbol{X}}_t$ and the variance-covariance matrix of ensemble members $\widehat{\boldsymbol{V}}_t$ can be represented as follows:

$$\widehat{\boldsymbol{X}}_t = \frac{1}{N}\boldsymbol{X}_t\mathbf{1}_{N\times N} \tag{5}$$

$$\delta\boldsymbol{X}_t = \boldsymbol{X}_t - \widehat{\boldsymbol{X}}_t \tag{6}$$

$$\widehat{\boldsymbol{V}}_t = \frac{1}{N-1}\delta\boldsymbol{X}_t(\delta\boldsymbol{X}_t)^T \tag{7}$$

where N is the number of ensemble members, $\boldsymbol{X}_t$ is the N-dimensional matrix of state variables $\boldsymbol{x}_t$ of ensemble members as follows:

$$\boldsymbol{X}_t = \left(\boldsymbol{x}_t^{(1)} \quad \boldsymbol{x}_t^{(2)} \quad \cdots \quad \boldsymbol{x}_t^{(N)}\right) \tag{8}$$

In addition, $\mathbf{1}_{N\times N}$ represents the $N\times N$ matrix of which the elements are 1.

$$\mathbf{1}_{N\times N} = \begin{pmatrix} 1 & 1 & \cdots & 1 \\ 1 & 1 & & \vdots \\ \vdots & & \ddots & \vdots \\ 1 & \cdots & \cdots & 1 \end{pmatrix} \tag{9}$$

In the above equations, superscripts (1), (2),⋯, (N) represent the indexes of ensemble members, N is the number of ensemble members, and superscript T represents the transposed matrix.

The variables of the ETKF are shown as follows:

$$\boldsymbol{W}_t = \begin{pmatrix} \boldsymbol{w}_t^{(1)} & \boldsymbol{w}_t^{(2)} & \cdots & \boldsymbol{w}_t^{(N)} \end{pmatrix} \tag{10}$$

$$\widehat{\boldsymbol{R}}_t = \frac{1}{N-1}\boldsymbol{W}_t{\boldsymbol{W}_t}^T \tag{11}$$

$$\boldsymbol{Y}_t = \begin{pmatrix} \boldsymbol{y}_t^{(1)} & \boldsymbol{y}_t^{(2)} & \cdots & \boldsymbol{y}_t^{(N)} \end{pmatrix} \tag{12}$$

$$\boldsymbol{H}_t = \begin{pmatrix} & 1 & & \\ & & & 1 \\ 1 & & 1 & \\ & & & \end{pmatrix} \tag{13}$$

where $\boldsymbol{W}_t$ represents the N-dimensional matrix of experimental noise of ensemble members $\boldsymbol{w}_t^{(i)}$ $(i = 1, \cdots N)$, $\widehat{\boldsymbol{R}}_t$ represents the variance-covariance matrix of experimental noise, $\boldsymbol{Y}_t$ represents the N-dimensional matrix of experimental values of ensemble members $\boldsymbol{y}_t^{(i)}(i = 1, \cdots N)$, and $\boldsymbol{H}_t$ represents the observation matrix of $l \times k$ dimension (l: number of experimental data, k: number of state variables) used to extract state variables at measurement locations from $\boldsymbol{X}_t$. $\boldsymbol{y}_t$ consists of 159 wing surface pressures and is same for each ensemble member. The procedure of the ETKF is expressed as follows:

$$\boldsymbol{I} + \delta{\boldsymbol{X}_t}^T{\boldsymbol{H}_t}^T\left[(N-1)\widehat{\boldsymbol{R}}_t\right]^{-1}\boldsymbol{H}_t\delta\boldsymbol{X}_t = \boldsymbol{Z}\boldsymbol{\Sigma}\boldsymbol{Z}^T \tag{14}$$

$$\widehat{\boldsymbol{R}}_t = \delta\boldsymbol{X}_t\boldsymbol{Z}\boldsymbol{\Sigma}^{-1}\boldsymbol{Z}^T\delta{\boldsymbol{X}_t}^T{\boldsymbol{H}_t}^T\left[(N-1)\widehat{\boldsymbol{R}}_t\right]^{-1} \tag{15}$$

$$\boldsymbol{T} = \boldsymbol{Z}\boldsymbol{\Sigma}^{-1/2}\boldsymbol{Z}^T \tag{16}$$

$$\widehat{\boldsymbol{X}}_t = \widehat{\boldsymbol{X}}_t + \widehat{\boldsymbol{K}}_t\left(\boldsymbol{Y}_t - \boldsymbol{H}_t\widehat{\boldsymbol{X}}_t\right) \tag{17}$$

$$\delta\boldsymbol{X}_t = \delta\boldsymbol{X}_t\boldsymbol{T} \tag{18}$$

$$\boldsymbol{X}_t = \widehat{\boldsymbol{X}}_t + \delta\boldsymbol{X}_t \tag{19}$$

where $\widehat{\boldsymbol{K}}_t$ represents the Kalman gain, and $\boldsymbol{I}$ in Eq. (14) represents the unit matrix. Superscripts -1 in Eqs. (14) and (15) indicate the inverse matrix and superscript $-1/2$ in Eq. (16) shows the square root of the inverse matrix. The singular value decomposition method was employed to calculate the inverse matrix and Eq. (14).

The angle of attack, the Mach number, and turbulent viscosity of each ensemble member are filtered by using the 159 wing surface pressures and the computational results of ensemble members through Eqs. (14) – (19).

4 DATA ASSIMILATION PROCEDURE

The procedure of the ETKF are summarized as follows:

1. Determine initial ensemble members $\left\{\boldsymbol{x}_0^{(i)}\right\}_{i=1}^{N}$ and $t^* \leftarrow 1$. (See subsection 1 for more details.)
2. At t^*
   (Prediction step)
   A) Calculate $\boldsymbol{x}_t^{(i)} = f_t\left(\boldsymbol{x}_{t-1}^{(i)}\right)$ for each ensemble member. (See subsection 2 for more details.)
   (Filtering step)
   B) Generate experimental noise $\left\{\boldsymbol{w}_t^{(i)}\right\}_{i=1}^{N}$.
   C) Calculate Eqs. (14) – (19) for the ETKF.
   (Post-processing)
   D) Modify negative turbulent viscosity filtered by the ETKF. (See subsection 3 for more details.)
3. Set $t^* \leftarrow t^* + 1$ and repeat step 2.
4. Calculate $\hat{\boldsymbol{x}}_t = f_t(\hat{\boldsymbol{x}}_{t-1})$. (See subsection 4 for more details.)

where t^* shows the number of executions of data assimilation. The experimental noise of ensemble members were set to be normal random number of $N(0,1.d\text{-}4)$, and the execution of the ETKF was repeated 45 times.

4.1 Setting of a set of ensemble members

The ETKF requires variation of state variables of ensemble members. This variation means uncertainty of computations. Several methods to realize the variation are available, such as assigning different boundary conditions or different initial conditions to each ensemble member. In this study, different angle of attack, different Mach number, and different values of Karman constant κ, which is a common constant of 0.41 between the SA model and the SST model, were assigned to computational conditions of ensemble members. Table 3 shows the computational conditions assigned to ensemble members. The number of ensemble members was set to 40, and the assigned values were determined equally from the ranges shown in Table 3 by the Latin hypercube sampling method [11]. The computations to obtain a set of ensemble members were conducted with the SA model and numerical schemes as shown in Table 1. As computational conditions were different in each ensemble member, each computed result was different.

Table 3: Computational conditions assigned to ensemble members

Computational condition	Range
Angle of attack [°]	5.57 – 6.55
Mach number	0.791 – 0.890
Karman constant	0.213 – 0.605

4.2 Prediction step

As described in section 3.1, the FaSTAR was employed as the system model of the prediction step. Here, the procedure of the prediction step had a difference between before

and after the first filtering step.

Before the first filtering step, all state variables defined in Eq. (3) were computed by the FaSTAR. Then the state variables defined in Eq. (3) of ensemble members were filtered through the filtering step.

After the first filtering step, the density, velocity components, and pressure filtered by the ETKF were computed in the prediction step. On the other hand, the angle of attack, Mach number, and turbulent viscosity filtered by the ETKF were fixed during the prediction step after the first filtering step.

The difference of the procedure of the prediction step between before and after the first filtering step arose from the following two concerns.

The first was that there was no guarantee whether the angle of attack, the Mach number, and turbulent viscosity filtered by only one-time data assimilation are best or not. Therefore, the several-time filtering steps were required to obtain better data assimilation result, and the prediction step was required to propagate the angle of attack, the Mach number, and turbulent viscosity filtered by the ETKF to the computational data.

The second was that the filtered primitive variables of the Navier–Stokes equations–density, velocity components, and pressure–were not suitable to satisfy the conservation law. Therefore, after the filtering step, the density, velocity components, and pressure were re-computed by the FaSTAR. This prediction step modified the filtered primitive variables so as to satisfy the conservation law.

The prediction step was conducted with the calculation steps of 400 and the CFL number of 50.

4.3 Post-processing Prediction step

The post-processing was required to avoid numerical divergence. Although the filtering step yielded realistic data combining experimental data and computational data, the filtering step had a potentially detrimental effect on the prediction step. Especially in this study, negative turbulent viscosity obtained through the filtering step caused the numerical divergence in the prediction step. To resolve the negative effect of the filtering step to the prediction step, several approaches are available [12]. In this study, as a simple way, the filtered turbulent viscosity less than 1.d-5 were replaced by the absolute value.

4.4 Re-calculation

After the angle of attack, the Mach number, and the turbulent viscosity of each ensemble member were filtered by the ETKF, the mean of the filtered flows was recalculated until the mean of the filtered flows converged. In the recalculation, the ensemble means of the filtered angle of attacks, the filtered Mach numbers, and the filtered turbulent viscosity were fixed. The recalculation was conducted with the CFL number of 50.

5 RESULTS AND DISCUUSIONS

5.1 Comparison of pressure coefficients on the wing surface

Before evaluating the estimated angle of attack, the estimated Mach number, and the estimated turbulent viscosity, the computed pressure coefficient with the estimated angle of

attack, the estimated Mach number, and the estimated turbulent viscosity are compared with the experiment. Figure 5 shows a comparison of pressure coefficients on the wing surface at the seven wing sections shown in Table 2.

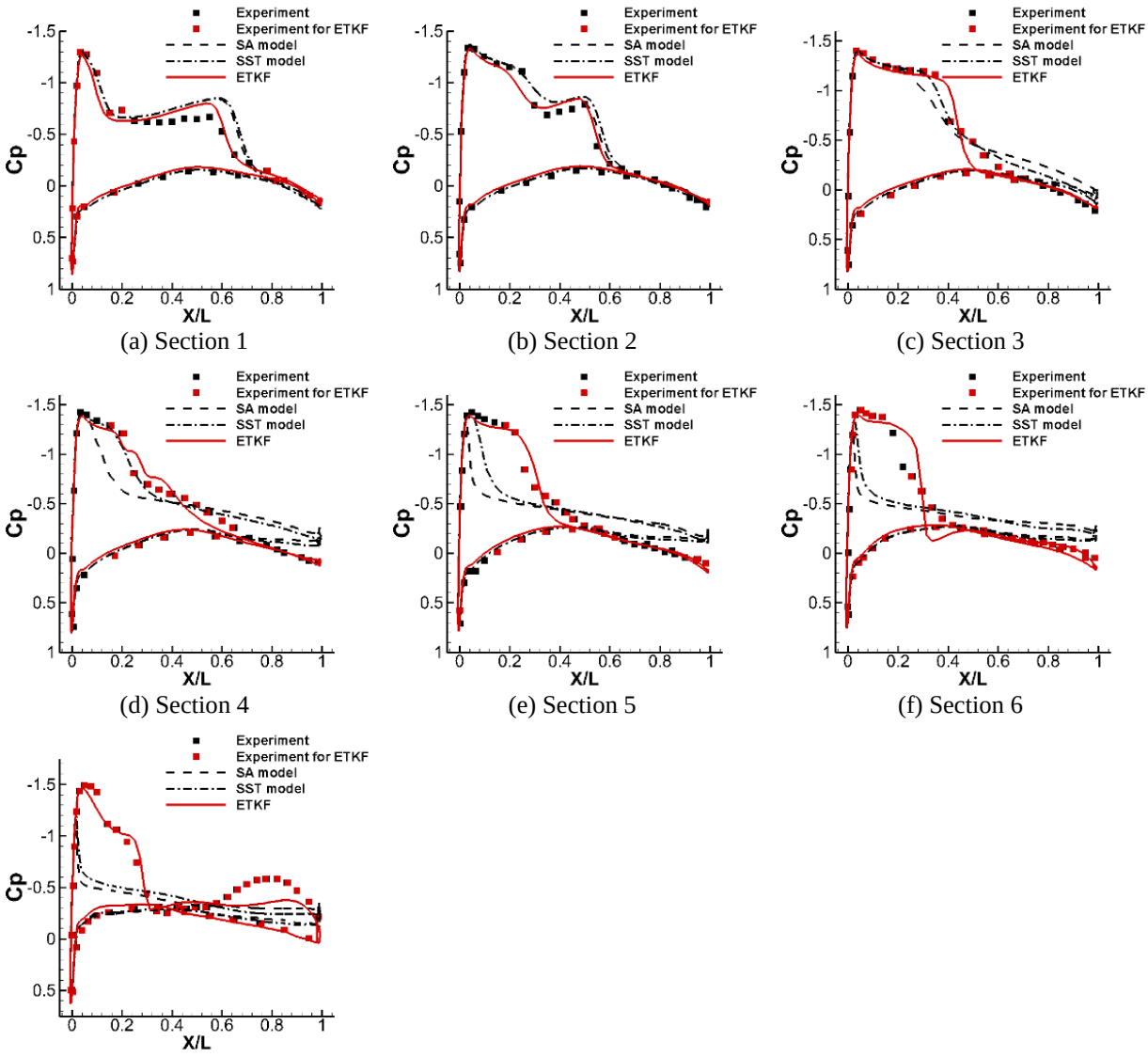

(a) Section 1 (b) Section 2 (c) Section 3

(d) Section 4 (e) Section 5 (f) Section 6

(g) Section 7

Figure 5: Comparison of pressure coefficients at the seven wing sections

In the figure at each section, the black square shows the original experimental data, the red square shows the experimental data employed for the ETKF. In addition, the black dash and the black dash dot lines show the computed pressure coefficients with the original angle of attack, the Mach number, and turbulence models of the SA model and the Menter SST model, and the red line shows the computed pressure coefficient with the estimated angle of attack, the estimated Mach number, and the estimated turbulent viscosity by the ETKF. Slight differences of locations between original experimental data and experimental data employed

for the ETKF in each figure show differences between computational grid points and measurement locations.

The comparison shows that the pressure coefficients of the ETKF agree better with the experiment at all sections than those of the SA and SST models. We see that the ETKF estimates the experimental pressure coefficients around the wing tip where there are major differences between the original computations and the experiment more properly than the original computations. These observations suggest that the ETKF can estimate the more proper angle of attack, the more proper Mach number, and the more proper turbulent viscosity than the originals.

5.2 Comparison of angle of attacks

Figure 6 shows histograms of the initial angle of attacks before data assimilation and of the angle of attacks filtered by the ETKF. The initial angle of attacks were set to be distributed equally in the range from 5.57° to 6.55° as shown in section 4.1. In addition, Table 4 shows means and standard deviations of the initial angle of attacks and of the angle of attacks filtered by the ETKF.

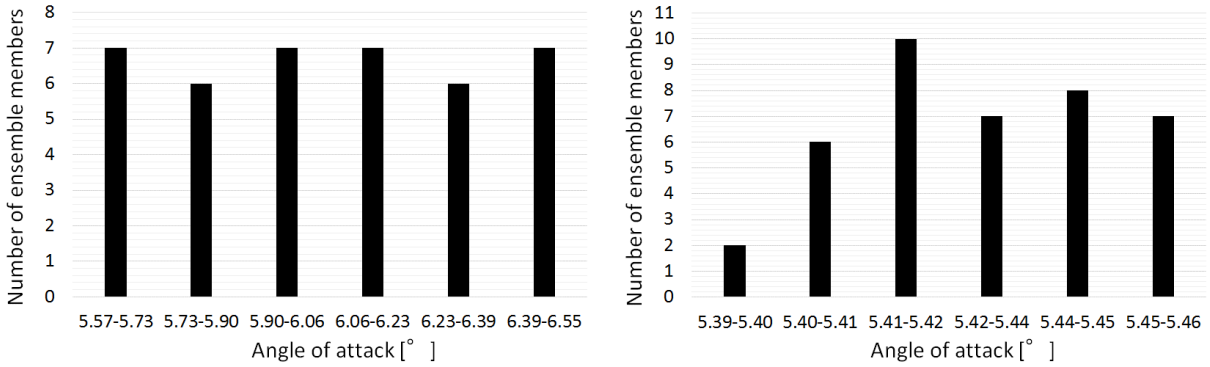

(a) Initial (before the estimation) (b) ETKF (after the estimation)

Figure 6: Histograms of the angle of attacks between before and after the ETKF

Table 4: Mean and standard deviation of the angle of attacks between before and after the ETKF

Mean of the angle of attacks [°]		Standard deviation of the angle of attacks [°^{2}]	
Initial	ETKF	Initial	ETKF
6.06	5.43	2.94d-01	1.93d-02

The comparison of angle of attacks between before and after the ETKF shows that (1) angle of attacks filtered by the ETKF converge to the smaller range from the initial range and (2) the ETKF estimates smaller angle of attack than the original angle of attack of 6.06°. The difference between the original angle of attack and the estimated angle of attack by the ETKF suggests that the original correction for the angle of attack of experiment is not sufficient to eliminate wind tunnel wall interference.

5.3 Comparison of the Mach numbers

Figure 7 shows histograms of the initial Mach numbers before data assimilation and the Mach numbers filtered by the ETKF. The initial Mach numbers were set to be distributed equally in the range from 0.79 to 0.89 as shown in section 4.1. In addition, Table 5 shows means and standard deviations of the initial Mach numbers and the filtered Mach numbers by the ETKF.

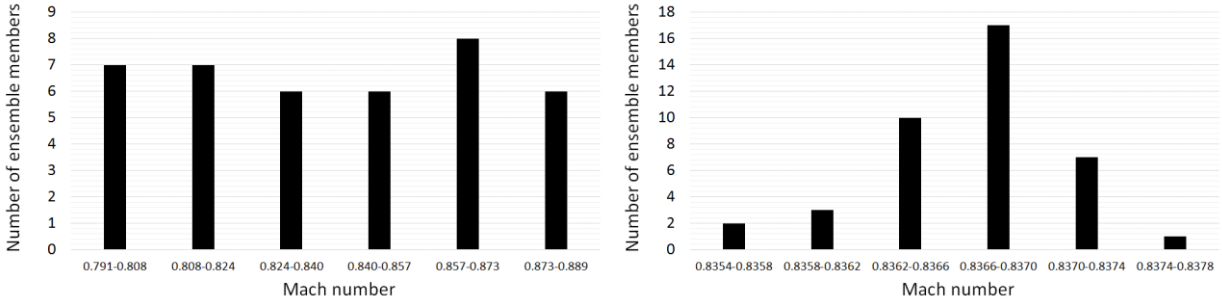

(a) Initial (before the estimation) (b) ETKF (after the estimation)

Figure 7: Histograms of the Mach numbers between before and after the ETKF

Table 5: Mean and standard deviation of the Mach numbers between before and after the ETKF

Mean of the Mach numbers		Standard deviation of the Mach numbers	
Initial	ETKF	Initial	ETKF
0.8395	0.8369	2.949d-2	3.612d-4

Figure 7 shows that the Mach numbers filtered by the ETKF converge to the smaller range from the initial larger range, as well as the filtered angle of attacks. Table 5 shows that the ETKF estimates almost the same Mach number as the original Mach number of 0.8395. In addition, the comparison between the filtered angle of attacks and the filtered Mach numbers shows that the filtered angle of attacks are distributed in the wider range than that of the filtered Mach numbers. This suggests that the angle of attack has less effect on the flow field than the Mach number.

5.4 Comparison of turbulent viscosity

Figure 8 shows a comparison of turbulent viscosity. In Fig. 8, (a) SA model and (b) SST model show the computed turbulent viscosity by the turbulence models, and (c) ETKF shows the mean of the filtered turbulent viscosity of ensemble members by the ETKF. And, the computations of SA and SST model were conducted with the original angle of attack of 6.06° and the original Mach number of 0.8395, the computation of ETKF was conducted with the estimated angle of attack of 5.43° and the Mach number of 0.8369. These figures are viewed from upstream side.

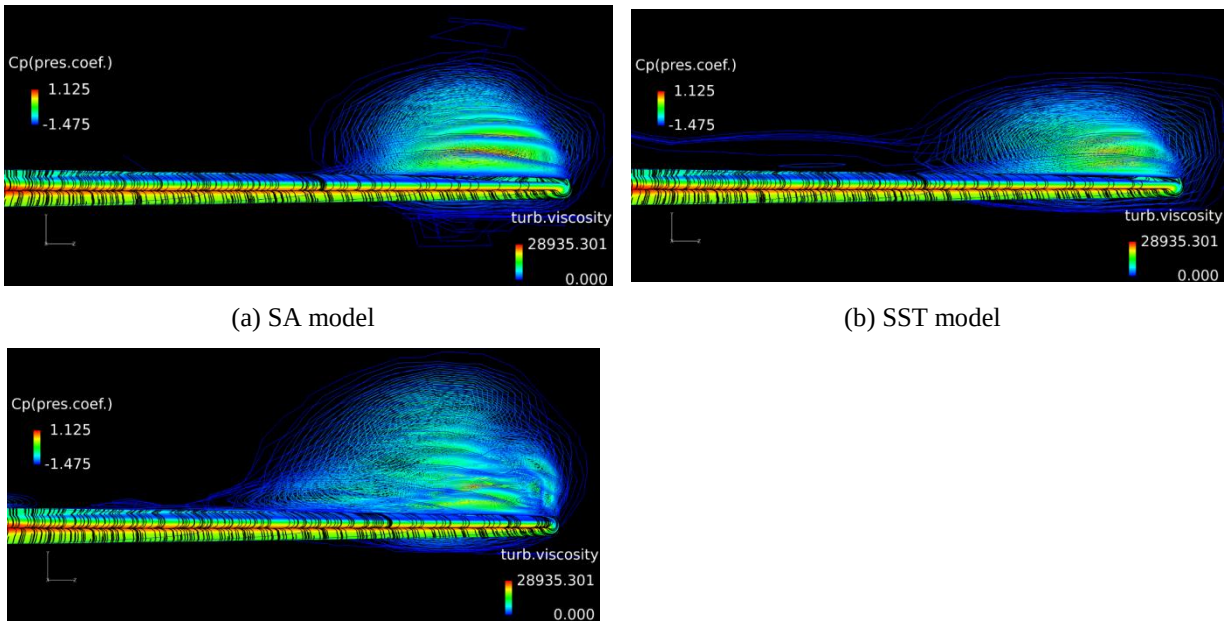

(a) SA model

(b) SST model

(c) ETKF

Figure 8: Comparison of turbulent viscosity.

It is confirmed from Fig. 8 that (1) the ETKF estimates the larger turbulent viscosity around the wing tip than those computed by the SA and SST models and (2) the ETKF estimates the larger turbulent viscosity at the center area of the wing than those computed by the SA and SST models. These observations suggest that the difference of turbulent viscosity between the two turbulence models and the ETKF at the two locations, the central area of the wing and the wing tip, has a large impact to represent the flow corresponding with the experimental pressure coefficient.

6 CONCLUSIONS

In this study, the ETKF was employed to estimate the angle of attack, the Mach number, and the turbulent viscosity corresponding with the experimental pressure coefficients of the transonic flow around the ONERA M6 wing. For the estimation, the 159 wing surface pressures from the AGARD advisory report and the fast aerodynamic routines, which is a CFD solver developed in Japan Aerospace Exploration Agency, were employed. As the results, the ETKF estimates (1) the lower angle of attack than the original, (2) almost the same Mach number as the original, and (3) stronger turbulent viscosity around the wing tip and around the center area of the wing than those computed by the SA model and the SST model. In addition, the computed result with the angle of attack, the Mach number, and the turbulent viscosity estimated by the ETKF showed the better agreement with the experimental pressure coefficients on the wing surface than the original computations. Therefore, it was found that the angle of attack, the Mach number and the turbulent visocity estimated by the ETKF were more proper than the originals and those computed by the SA model and the SST model.

This study suggested that the ETKF estimated the proper angle of attack, the proper Mach

number, and the proper turbulent viscosity based on the experimental surface pressures. In the future, the proper angle of attack and the proper Mach number estimated by data assimilation can yield useful suggestions to set proper computational boundary conditions that to date have been set empirically. In addition, the proper turbulent viscosity estimated by data assimilation will contribute to design the next best eddy viscosity type turbulence model, because current computational and experimental approaches have difficulties in representing turbulent viscosity in complex turbulent flows.

REFERENCES

[1] R.E. Kalman, A new approach to linear filtering and prediction problems. *Journal of Basic Engineering*, (1960) vol. 82, no. 1, pp. 34-45.
[2] R. Dalay, Atmospheric Data Analysis, Cambridge University Press, (1994).
[3] C. Wunsch, The Ocean Circulation Inverse Problem, Cambridge University Press, (1996).
[4] C.H. Bishop, B.J. Etherton, and S.J. Majumdar, Adaptive sampling with the ensemble transform Kalman Filter. Part I: Theoretical aspects, *MONTHLY WEATHER REVIEW*, (2001) Vol. 129, pp. 420-436.
[5] P.R. Spalart, A one-equation turbulence model for aerodynamic flows, AIAA paper 1992-439, (1992).
[6] F.R. Menter, et al., Ten Years of Industrial Exrience with the SST Turbulence Model, Turbulence, Heat and Mass Transfer 4, Begell House, Inc., (2003).
[7] A. Hashimoto, et al., Toward the Fastest Unstructured CFD Code 'FaSTAR', AIAA 2012-1075, (2012).
[8] S. Obayashi, G.P. Guruswamy, Convergence Acceleration of a Navier-Stokes Solver for Efficient Static Aeroelastic Computation, *AIAA Journal*, (1995) vol. 33, no. 6, pp. 1134-1141.
[9] E. Shima, K. Kitamura, and K. Fujimoto, New Gradient Calculation Method for MUSCL Type CFD Schemes in Arbitrary Polyhedra, AIAA Paper 2010-1081, (2010).
[10] V. Schmitt and F. Charpin, PRESSURE DISTRIBUTIONS ON THE ONERA-M6-WING AT TRANSONIC MACH NUMBERS, AGARD Report AR 138, (1979).
[11] M.D. Kay, R.J. Beckman, and W.J. Conover, A Comparison of Three Methods for Selecting Values of Input Variables in the Analysis of Output from a Computer Code, *Technometrics*, (1979) vol. 21, no. 2, pp. 239-245.
[12] T. Janjić, D. Mclaughlin, S.E. Cohn, and M. Verlaan, Conservation of Mass and Preservation of Positivity with Ensemble-Type Kalman Filter Algorithms, *MONTHLY WEATHER REVIEW*, (2014) vol. 142, no. 2, pp. 755-773.